We are IntechOpen, the world's leading publisher of Open Access books Built by scientists, for scientists

6,900
Open access books available

185,000
International authors and editors

200M
Downloads

Our authors are among the

154
Countries delivered to

TOP 1%
most cited scientists

12.2%
Contributors from top 500 universities



WEB OF SCIENCE™

Selection of our books indexed in the Book Citation Index in Web of Science™ Core Collection (BKCI)

Interested in publishing with us?
Contact book.department@intechopen.com

Numbers displayed above are based on latest data collected.
For more information visit www.intechopen.com



13

Three-Scale Structure Analysis Code and Thin Film Generation of a New Biocompatible Piezoelectric Material $MgSiO_3$

Hwisim Hwang, Yasutomo Uetsuji and Eiji Nakamachi
Doshisha University
Japan

1. Introduction

In this study, three subjects were investigated for a new biocompatible piezoelectric material generation:

1. Development of a numerical analysis scheme of a three-scale structure analysis and a process crystallographic simulation.
2. Design of new biocompatible piezoelectric materials.
3. Generation of $MgSiO_3$ thin film by using radio-frequency (RF) magnetron sputtering system.

Until now, lead zirconate titanate ($Pb(Zr,Ti)O_3$: PZT) has been used widely for sensors (Hindrichsena et al., 2010), actuators (Koh et al., 2010), memory devices (Zhang et al., 2009) and micro electro mechanical systems (MEMS) (Ma et al., 2010), because of its high piezoelectric and dielectric properties. The piezoelectric thin film with aligned crystallographic orientation shows the highest piezoelectric property than any polycrystalline materials with random orientations. Sputtering (Bose et al., 2010), chemical or physical vapor deposition (CVD or PVD) (Tohma et al., 2002), pulsed laser deposition (PLD) (Kim et al., 2006) and molecular beam epitaxy (MBE) (Avrutin et al., 2009) are commonly used to generate high performance piezoelectric thin films. Lattice parameters and crystallographic orientations of epitaxially grown thin films on various substrates can be controlled by these procedures. K. Nishida et al. (Nishida et al., 2005) generated [001] and [100]-orientated PZT thin films on MgO(001) substrate by using CVD method. They succeeded to obtain a huge strain caused by the two effect: the synergetic effect of [001] orientation with the piezoelectric strain; and the strain effect of [100] orientation caused by switching under conditions of the external electric field. Additionally, PZT-based piezoelectric materials, such as $Pb(Zn_{1/3}Nb_{2/3})O_3$-$PbTiO_3$ (Geetika & Umarji, 2010) and $PbMg_{1/3}Nb_{2/3}O_3$-$PbTiO_3$ (Kim et al., 2010), have also been developed.

However, lead, which is a component of PZT-based piezoelectric material, is the toxic material. The usage of lead and toxic materials is prohibited by the waste electrical and electronic equipment (WEEE) and the restriction on hazardous substances (RoHS).

For alternative piezoelectric materials of the PZT, lead-free piezoelectric materials have been studied. J. Zhu et al. (Zhu et al., 2006) generated [111]-orientated $BaTiO_3$ on $LaNiO_3$(111) substrate, which had a crystallographic orientation with maximum piezoelectric strain

constants. S. Zhang et al. (Zhang et al., 2009) doped Ca and Zr in $BaTiO_3$ and succeeded in generating the piezoelectric material with high piezoelectric properties. Further, P. Fu et al. (Fu et al., 2010) doped La_2O_3 in Bi-based $(Bi_{0.5}Na_{0.5})_{0.94}Ba_{0.06}TiO_3$ and succeeded in generating a high performance piezoelectric material. However, their goals were to develop an environmentally compatible piezoelectric material, and the biocompatibility of their piezoelectric materials has not been investigated. Therefore, their piezoelectric materials could not be applied for Bio-MEMS devices.

Recently, the Bio-MEMS, which can be applied to the health monitoring system and the drug delivery system, is one of most attractive research subject in the development of the nano- and bio-technology. Therefore, the biocompatible actuator for the micro fluidic pump in Bio-MEMS is strongly required. However, they remain many difficulties to design new biocompatible materials and find an optimum generation process. Especially, it is difficult to optimize the thin film generation process because there are so many process factors, such as the substrate material, the substrate temperature during the sputtering, the target material and the pressure in a chamber. Therefore, the numerical analysis scheme is necessary to design new materials and optimize the generation process.

The analysis scheme based on continuum theory is strongly required, due to time consuming experimental approach such as finding an optimum sputtering process and a substrate crystal structure through enormous experimental trials. The analysis scheme should predict the thin film deformation, strain and stress, which are affected by the imposed electric field and are constrained by the substrate.

Until now, the conventional analysis schemes, such as the molecular dynamics (MD) method (Rubio et al, 2003) and the first-principles calculation based on the density functional theory (DFT) (Lee & Chung, 2006), have been applied to the crystal growth process simulations. The MD method has been used mainly to analyze the crystal growth process of pure atoms. J. Xu et al. (Xu & Feng, 2002) calculated the Ge growth on Si(111). In the cases of the perovskite compounds, the MD method has been applied to analyze the phase transition, the polarization switching and properties of crystal depending on temperature and pressure. J. Paul et al. (Paul et al., 2007) analyzed the phase transition of $BaTiO_3$ caused by rising temperature and S. Costa et al. (Costa et al., 2006) analyzed the one of $PbTiO_3$ caused by rising temperature and pressure. However, the reliability of its numerical results is poor due to its uncertain inter-atomic potentials for the various combinations of atoms. The MD method could not predict the differences of poly-crystal structures and material properties caused by changing combinations of the crystals and the substrates. It can be concluded that the conventional MD method has many problems for the crystal growth prediction of perovskite compounds grown on the arbitrarily selected substrates.

On the other hand, the DFT can treat interactions between electrons and protons, therefore the reliable inter-atomic potentials can be obtained. The first-principles calculations based on the DFT were applied to the epitaxial growth of the ferroelectric material by O. Diegueaz et al. and I. Yakovkin et al.. O. Diegueaz et al. (Diegueaz et al., 2005) evaluated the stress increase and the polarization change caused by the lattice mismatch between a substrate and a thin film crystal, such as $BaTiO_3$ and $PbTiO_3$. Similarly, I. Yakovkin et al. (Yakovkin & Gutowski, 2004) has investigated in the case of $SrTiO_3$ thin film growth on Si substrate. However, these analyses adopted limited assumptions, such as fixing the conformations of thin film crystals and the growth orientations on the substrates. In this conventional algorithm, the grown orientation is determined by the purely geometrical lattice mismatch

between thin films and substrates. This algorithm is not sufficient to predict accurately the preferred orientation of the thin film.

In order to generate the new piezoelectric thin film, a crystal growth process of the thin film should be predicted accurately. The stable crystal cluster of the thin film, which consists geometrically with substrate crystal, is grown on the substrate. Generally, the crystal cluster is an aggregate of thin film crystals. Their morphology and orientations were varied according to the combination of the thin film and the substrate crystals. Therefore, the numerical analysis scheme of the crystal growth process, which can find the best combination of the thin film and the substrate crystal, is strongly required, to optimize the new piezoelectric thin film.

In this chapter, following contents are discussed to develop the new biocompatible $MgSiO_3$ piezoelectric thin film.

1. The three-scale structure analysis algorithm, which can design new piezoelectric materials, is developed.
2. The best substrate of the $MgSiO_3$ piezoelectric thin film is found by using the three-scale structure analysis code.
3. The $MgSiO_3$ thin film is grown on the best substrate by using the RF magnetron sputtering system, and piezoelectric properties are measured.
4. An optimum generating condition of the $MgSiO_3$ piezoelectric thin film is found by using the response surface method.

Section 2 provides the description to the algorithm of the three-scale structure analysis code on basis of the first-principles calculation, the process crystallographic simulation and the crystallographic homogenization theory. Section 3 provides the best substrate of the new biocompatible $MgSiO_3$ piezoelectric thin film calculated by the three-scale structure analysis code. In section 4, the optimum generating condition of $MgSiO_3$ piezoelectric thin film is found. Finally, conclusions are given in section 5.

2. A three-scale structure analysis code

This section describes the physical and mathematical modelling of the three-scale structure and the numerical analysis scheme of three-scale structure analysis to characterize and design epitaxially grown piezoelectric thin films. The existing two-scale finite element analysis is the effective analysis tool for characterization of existing piezoelectric materials. This is because virtually or experimentally determined crystal orientations can be employed for calculation of piezoelectric properties of the macro continuum structure (Jayachandran et al., 2009). However, it can not be applied to a new piezoelectric material, due to unknown crystal structure and material properties.

Figure 1 shows the schematic description of the three-scale modelling of a new piezoelectric thin film, which is grown on a substrate. It shows the three-scale structures, such as a “crystal structure”, a “micro polycrystalline structure” and a “macro continuum structure”. In the crystal structure analysis, stable structures and crystal properties are evaluated by using the first-principles calculation. Preferred orientations and their fraction are calculated by using the process crystallographic simulation in the micro polycrystalline structure analysis. The macro continuum structure analysis provides the piezoelectric properties of the thin film by using the finite element analysis on basis of the crystallographic homogenization theory. Therefore, the three-scale structure analysis can predict the epitaxial growth process of not only the existent piezoelectric materials but also the new ones.

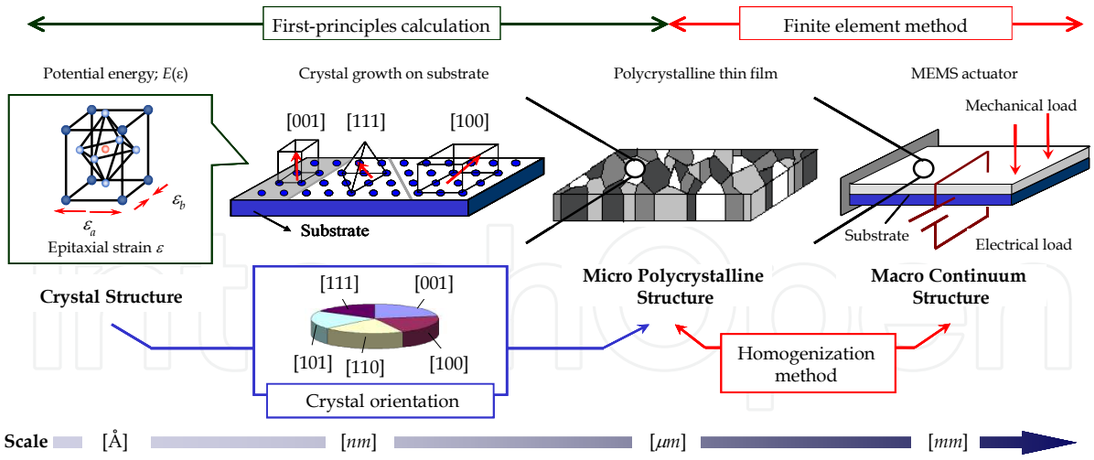


Fig. 1. Three-scale modelling of piezoelectric thin film as a process crystallography.

2.1 Crystal structure analysis by using the first-principles calculation

2.1.1 Stable crystal structure analysis

The stable structures of the perovskite cubic are calculated by the first-principles calculation based on the density functional theory (DFT) by using the CASTEP code (Segal et al., 2002). The stable structures are, then, computed using an ultra-soft pseudo potential method under the local density approximation (LDA) for exchange and correlation terms. A plane-wave basis set with 500eV cutoff energy is used and special k-points are generated by a 8x8x8 Monkhorst-pack mesh (Monkhorst et al., 1976).

The perovskite-type compounds ABX_3 provide well-known examples of displacive phase transitions. They are in a paraelectric non-polar phase at high temperature and have a cubic crystal structure (lattice constant $a = c$). The cubic crystal structure consists of A cations in the large eightfold coordinated site, B cations in the octahedrally coordinated site, and X anions at equipoint. The stability of cubic crystal structure can be estimated by an essential geometric condition, tolerance factor t. If ion radiuses of A, B and X are indicated with r_A, r_B, r_X, tolerance factor t can be described as

$$t = \frac{r_A + r_X}{\sqrt{2}\left(r_B + r_X\right)} \tag{1}$$

When tolerance factor t consists in the range from 0.75 to 1.10, the perovskite-type crystal structure has high stability. The cubic crystal structure often distorts to ferroelectric phase of lower symmetry at decreased temperature, which is a tetragonal crystal structure ($a > c$) with spontaneous polarization. These ferroelectric distortions are caused by a soft-mode of phonon vibration in cubic crystal structure, and it brings to good piezoelectricity. The soft-mode can be distinguished from other phonon vibration modes with negative eigenfrequency, and the transitional crystal structure depends strongly on the eigenvectors. Consequently, new biocompatible piezoelectric materials are searched according to the flowchart in Fig. 2. Firstly, biocompatible elements are inputted to A and B cations while halogens and chalcogens are set to X anion for the perovskite-type compounds. The combination of three elements is determined to satisfy the stable condition of the tolerance factor. The stable cubic structure of perovskite-type oxides is calculated to minimize the

total energy. Next, the phonon vibration in the stable cubic structure is analyzed to catch the soft-mode which causes a phase transition from the paraelectric non-polar phase (cubic structure) to the ferroelectric phase (tetragonal structure). When the eigenfrequency of phonon vibration is positive, it is considered that the cubic structure is the most stable phase and does not change to other phase. On the other hand, in case that the eigenfrequency is negative, the cubic structure is guessed to be an unstable phase and change to other phase corresponding to the soft-mode. Additionally, if all eigenvectors of constituent atoms are parallel to *c* direction in crystallographic coordinate system, it is supposed to change from cubic to tetragonal structure. If not, it is supposed to transit to other structures except tetragonal one. On the base of phonon properties, the stable tetragonal structure with minimum total energy is searched using the eigenvector components for the initial atomic coordinates.

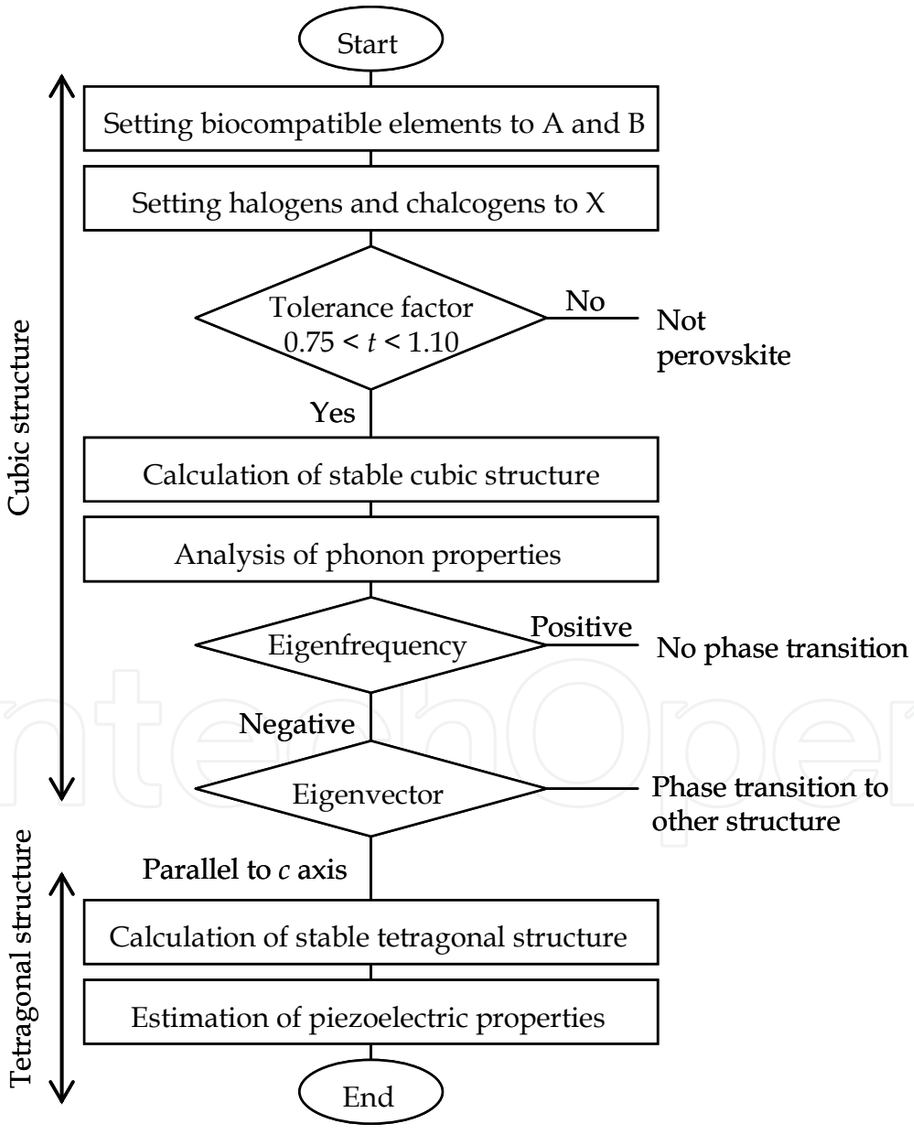


Fig. 2. The flowchart of searching new piezoelectric materials by the first-principles DFT.

Recently, many perovskite cubic crystals such as $SrTiO_3$ and $LaNiO_3$ have been reported. However, most of these materials could not be transformed into a tetragonal structure below Curie temperature, because most of perovskite cubic crystals are more stable than tetragonal crystals. Therefore, the tetragonal structure indicates a soft-mode of the phonon oscillation in cubic structure. Lattice parameters and piezoelectric constants of the tetragonal structure are calculated using the DFT.

2.1.2 Characterization of piezoelectric constants

The total closed circuit (zero field) macroscopic polarization of a strained crystal P_i^T can be described as,

$$P_i^T = P_i^S + e_{iv}\varepsilon_v \tag{2}$$

where P_i^S is the spontaneous polarization of the unstrained crystal (Szabo et al., 1998, 1999). Under Curie temperature, ferroelectric crystal with tetragonal structure has a polarization along the *c* axis. The three independent piezoelectric stress tensor components are $e_{31} = e_{32}$, e_{33} and $e_{15} = e_{24}$. $e_{31} = e_{32}$ and e_{33} describe the zero field polarization induced along the *c* axis, when the crystal is uniformly strained in the basal *a*-*b* plane or along the *c* axis, respectively. $e_{15} = e_{24}$ measures the change of polarization perpendicular to the *c* axis induced by the shear strain. This latter component is related to induced polarization by $P_1 = e_{15}\varepsilon_5$ and $P_2 = e_{15}\varepsilon_4$. The total induced polarization along *c* axis can be described by a sum of two contributions.

$$P_3 = e_{33}\varepsilon_3 + e_{31}(\varepsilon_1 + \varepsilon_2) \tag{3}$$

where $\varepsilon_1 = (a - a_0)/a_0$, $\varepsilon_2 = (b - b_0)/b_0$ and $\varepsilon_3 = (c - c_0)/c_0$ are strains along the *a*, *b* and *c* axes, respectively, and a_0, b_0 and c_0 are lattice parameters of the unstrained structure.

The electronic part of the polarization is determined using the Berry's phase approach (Smith & Vandelbilt, 1993), a quantum mechanical theorem dealing with a system coupled under the condition of slowly changing environment. One can calculate the polarization difference between two states of the same solid, under the necessary condition that the crystal remains an insulator along the path, which transforms the two states into each other through an adiabatic variation of a crystal Hamiltonian parameter λ_H. The magnitude of the electronic polarization of a system in state λ_H is defined only modulo $e\mathbf{R}/\Omega$, where $\mathbf{R}$ is a real-space lattice vector, Ω the volume of the unit cell, and *e* the charge of electron. In practice, the $e\mathbf{R}/\Omega$ factor can be eliminated by careful inspection, in the condition where the changes in polarization are described as $|\Delta P| << |e\mathbf{R}/\Omega|$. The electronic polarization can be described as,

$$P^{\mathrm{el}}(\lambda_H) = -\frac{2e}{(2\pi)^3}\int_{BZ} d\mathbf{k}\,\frac{\partial}{\partial \mathbf{k}'}\phi^{(\lambda_H)}(\mathbf{k},\mathbf{k}')\Big|_{\mathbf{k}'=\mathbf{k}} \tag{4}$$

where the integration domain is the reciprocal unit cell of the solid in state λ_H and $\phi^{(\lambda_H)}$ is quantum phase defined as phases of overlap-matrix determinants constructed from periodic parts of occupied valence Bloch states $\nu_n^{(\lambda_H)}(\mathbf{k})$ evaluated on a dense mesh of $\mathbf{k}$ points from $\mathbf{k}_0$ to $\mathbf{k}_0+\mathbf{b}$, where $\mathbf{b}$ is the reciprocal lattice vector.

$$\phi^{(\lambda_H)}(\mathbf{k},\mathbf{k}') = \mathrm{Im}\left\{\ln[\det\left\langle v_m^{(\lambda_H)}(\mathbf{k})\middle| v_m^{(\lambda_H)}(\mathbf{k}')\right\rangle]\right\} \tag{5}$$

The electronic polarization difference between two crystal states can be described as,

$$\Delta \boldsymbol{P}^{\mathrm{el}} = \boldsymbol{P}^{\mathrm{el}}(\lambda_{H2}) - \boldsymbol{P}^{\mathrm{el}}(\lambda_{H1}) \tag{6}$$

Common origins to determine electronic and core parts are arbitrarily assigned along the crystallographic axes. The individual terms in the sum depend on the choice, however, the final results are independent of the origins.
The elements of the piezoelectric stress tensor can be separated into two parts, which are a clamped-ion or homogeneous strain u , and a term that is due to an internal strain such as relative displacements of differently charged sublattices

$$\boldsymbol{e}_{i\nu} = \frac{\partial \boldsymbol{P}_i^T}{\partial \varepsilon_\nu}\bigg|_{\boldsymbol{u}} + \sum_k \frac{\partial \boldsymbol{P}_i^T}{\partial \boldsymbol{u}_{k,i}}\bigg|_{\varepsilon} \frac{\partial \boldsymbol{u}_{k,i}}{\partial \varepsilon_\nu} \tag{7}$$

where $\boldsymbol{P}_i^T$ is the total induced polarization along the ith axis of the unit cell.
Equation (7) can be rewritten in terms of the clamped-ion part and the diagonal elements of Born effective charge tensor.

$$\boldsymbol{e}_{i\nu} = \boldsymbol{e}_{i\nu}^{(0)} + \sum_k \frac{\boldsymbol{e}\boldsymbol{a}_i}{\Omega} \boldsymbol{Z}_{k,ii}^* \frac{\partial \boldsymbol{u}_{k,i}}{\partial \varepsilon_\nu} \tag{8}$$

where a_i is the lattice parameter, the clamped-ion term $e^{(0)}$ is the first term of Eq. (8). $e^{(0)}$ is equal to the sum of rigid core $e^{(0)}$, core and valence electronic $e^{(0),\mathrm{el}}$ contributions. Subscript k corresponds to the atomic sublattices. Z^* is the Born effective charge described as,

$$\boldsymbol{Z}_{k,i\nu}^* = \boldsymbol{Z}_k^{core} + \boldsymbol{Z}_{k,i\nu}^{*,\mathrm{el}} = \frac{\Omega}{\boldsymbol{e}\boldsymbol{a}_i} \frac{\partial \boldsymbol{P}_i}{\partial \boldsymbol{u}_{k,\nu}}\bigg|_{\varepsilon} \tag{9}$$

Piezoelectric response includes two contributions, that appear in linear response for finite distortional wave vectors **q**, and contributions which appear at **q**= 0. Improper polarization changes arise from the rotation or dilation of the spontaneous polarization $\boldsymbol{P}_i^s$. The proper polarization of a ferroelectric or pyroelectric material is given by

$$\boldsymbol{P}_i^P = \boldsymbol{P}_i^T - \sum_j \left(\varepsilon_{ij}\boldsymbol{P}_j^s - \varepsilon_{jj}\boldsymbol{P}_i^s\right) \tag{10}$$

Proper piezoelectric constants $\boldsymbol{e}_{i\nu}^P$ can be described as,

$$\boldsymbol{e}_{31}^P = \frac{\partial \boldsymbol{P}_3^T}{\partial \varepsilon_1} + \boldsymbol{P}_3^s \tag{11}$$

$$\boldsymbol{e}_{15}^P = \frac{\partial \boldsymbol{P}_1^T}{\partial \varepsilon_5} - \boldsymbol{P}_3^s \tag{12}$$

and $e_{33}^{P} = e_{33}^{T}$, because the improper part of e_{33}^{T} is zero. The difference between proper polarization and total one is due to only homogeneous part, which can be described in the following equation for e_{31} ($e_{31}^{P,\mathrm{hom}}$).

$$e_{31}^{P,\mathrm{hom}} = e_{31}^{\mathrm{hom}} + P_3^{s} = \frac{\partial P_3^{\mathrm{el},T}}{\partial \varepsilon_1} + P_3^{\mathrm{el},s} \tag{13}$$

This equation can use the similar expression for $e_{15}^{P,\mathrm{hom}}$. The homogeneous part appears as a pure electronic term in the expression for the proper piezoelectric constants, which differ in crystal with nonzero polarization in the unstrained state.

The first term in Eq. (8) can be evaluated by polarization differences as a function of strain, with the internal parameters kept fixed at their values corresponding to zero strain. The second term, which arises from internal microscopic relaxation, can be calculated after determining the elements of the dynamical transverse charge tensors and variations of internal coordinate u_i as a function of strain. Generally, transverse charges are mixed second derivatives of a suitable thermodynamic potential with respect to atomic displacements and electric field. They evaluate the change in polarization induced by unit displacement of a given atom at the zero electric field to linear order. In a polar insulator, transverse charges indicate polarization increase induced by relative sublattice displacement. While many ionic oxides have Born effective charges close to their static value, ferroelectric materials with perovskite structure display anomalously large dynamical charges.

2.2 Micro polycrystalline structure analysis by using the process crystallographic simulation

2.2.1 Evaluation method of the total energy

The tetragonal crystal structure of perovskite compound and its five typical orientations [001], [100], [110], [101] and [111] are shown in Fig. 3. Considering a epitaxial growth of the crystal on a substrate, the lattice constants including a, b, c, θ_{ab}, θ_{bc} and θ_{ca} are changed because of the lattice mismatch with the substrate. These crystal structure changes can be determined by considering six components of mechanical strain in crystallographic coordinate system such as ε_a, ε_b, ε_c, γ_{ab}, γ_{bc} and γ_{ca}. In a general analysis procedure, the lattice mismatch in the specific direction was calculated and the crystal growth potential was derived. However, the epitaxially grown thin film crystal is in a multi-axial state. Therefore, the numerical results of the crystal energy of thin films are not corrected when considering only uni-axis strain.

In this study, the total energy of a crystal thin film with multi-axial crystal strain states is calculated by using the first-principles calculation, and is applied to the case of the epitaxial growth process. An ultra-soft pseudo-potentials method is employed in the DFT with the condition of the LDA for exchange and correlation terms. Total energies of the thin film crystal as the function of six components of crystal strain are calculated to find a minimum value. Total energies are calculated discretely and a continuous function approximation is introduced. A sampling area is selected by considering the symmetry between a and b axes in a tetragonal crystal structure. Sampling points are generated by using a latin hypercube sampling (LHS) method (Olsson & Sandberg, 2002), which is the efficient tool to get nonoverlap sapling points. The following global function model is generated by using a kriging polynomial hybrid approximation (KPHA) method (Sakata et al., 2007).

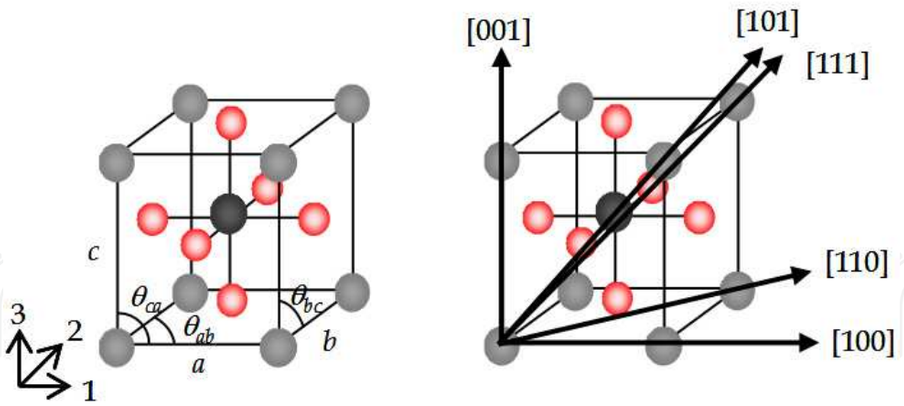


Fig. 3. Crystal structure and orientations of perovskite compounds.

$$E = A_h \varepsilon_h^2 + B_{ij} \varepsilon_i \varepsilon_j + C_l \varepsilon_l + E_{T0} \quad (h,i,j = a,b,c,ab,bc,ca) \tag{14}$$

where E_{T0} is the total energy of the stable crystal, ε_h, ε_i and ε_j epitaxial strains and A_h, B_{ij} and C_l coefficients generated by KPHA method. A gradient of total energy at each sampling point is calculated to generate an approximate quadratic function. The minimum point of a total energy can be found by using this function.

2.2.2 Algorithm of the process crystallographic simulation

In the process crystallographic simulation, it is assumed that several crystal unit cells of crystal clusters, which have certain conformations, can grow on a substrate as shown Fig. 4. The left-hand side diagram in Fig. 4 shows an example of conformation in cases of [001], [100], [110] and [101] orientations, and the right-hand side shows [111] orientation. O, A and B are points of substrate atoms corresponding to thin films ones within the allowable range of distance. l_{OA} and l_{OB} indicate distances of A and B from O, respectively. θ_{AOB} indicates the angle between lines OA and OB.

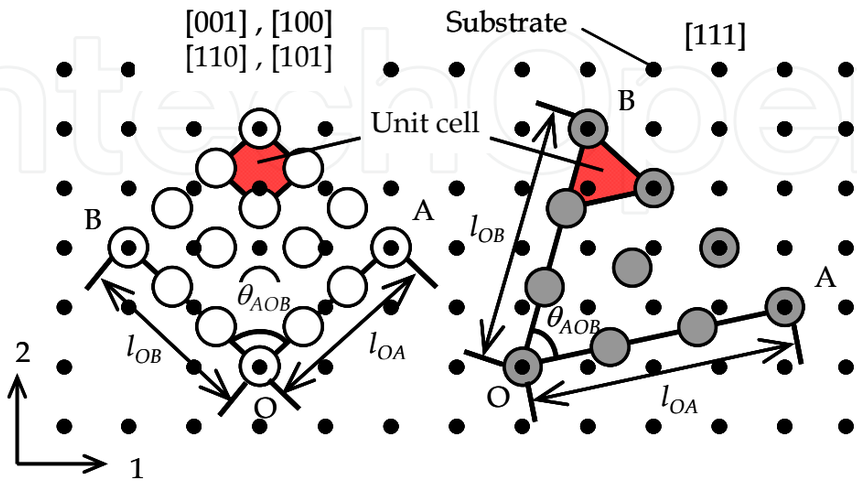


Fig. 4. Schematic of crystal conformations on a substrate.

	[001]	[100]	[110]	[101]	[111]
l_{OA}	a	c	c	$\sqrt{a^2+c^2}$	$\sqrt{a^2+c^2}$
l_{OB}	b	b	$\sqrt{a^2+b^2}$	b	$\sqrt{b^2+c^2}$
Epitaxial strain					
ε_a	$\frac{l_{OA}}{ka}-1$	ε_a^*	ε_a^*	ε_a^*	$\frac{\sqrt{(l_{OA}/k)^2-c^2(1+\varepsilon_c)^2}}{a}-1$
ε_b	$\frac{l_{OB}}{kb}-1$	$\frac{l_{OB}}{kb}-1$	$\frac{\sqrt{(l_{OB}/k)^2-a^2(1+\varepsilon_a^*)^2}}{b}-1$	$\frac{l_{OB}}{kb}-1$	$\frac{\sqrt{(l_{OB}/k)^2-c^2(1+\varepsilon_c)^2}}{b}-1$
ε_c	ε_c^*	$\frac{l_{OA}}{kc}-1$	$\frac{l_{OA}}{kc}-1$	$\frac{\sqrt{(l_{OA}/k)^2-a^2(1+\varepsilon_a^*)^2}}{c}-1$	$\frac{k-1}{kc}\sqrt{l_{OA}l_{OB}\cos\theta_{AOB}}-1$
γ_{ab}		γ_{ab}^*	γ_{ab}^*	$\theta_{AOB}-\theta_{ab}$	γ_{ab}^*
γ_{bc}	γ_{bc}^*	γ_{bc}^*	$\theta_{AOB}-\theta_{bc}$	γ_{bc}^*	$\frac{b}{c}\gamma_{ab}^*$
γ_{ca}	γ_{ca}^*	$\theta_{AOB}-\theta_{ca}$	$\theta_{AOB}-\theta_{ca}$	$\frac{a}{c}\gamma_{ab}$	$\frac{a}{c}\gamma_{ab}^*$

ε_i^* and γ_{ij}^* can be given from first-principles calculation to the minimize total energy

Table 1. Relationship of lattice constants and epitaxial strain with crystal orientations.

Table 1 summarizes the relationship between the lattice constants of the thin film and l_{OA} and l_{OB} according to crystal orientations. Additionally, Table 1 shows crystal strains, which can be determined in the corresponded crystal orientations. However, particular crystal strains, such as ε_i^* and γ_{ij}^*, cannot be determined by employing the lattice constants of the thin film and the geometric constants of the substrate. In this numerical analysis scheme, their unknown components are determined by employing the condition of minimum total energy of the crystal unit cell.

Figure 5 shows the flowchart of the crystal growth prediction algorithm. First, lattice constants of the thin film and the substrate are inputted. The following procedure is demonstrated. Substrate coordinates of A and B points, which are indicated as (m_A, n_A) and (m_B, n_B), are updated according to the numerical result under the condition of fixing O point in order to generate candidate crystal clusters with assumed conformations and orientations. The search range of the crystal cluster is settled as $0 < m_A, m_B < m$ and $0 < n_A, n_B < n$ by considering the grain size of the piezoelectric thin film crystal. $\vec{e}_1$ and $\vec{e}_2$ as shown in Figure 5 are unit vectors of the substrate coordinate system. Lattice constants of the crystal cluster are compared with geometrical parameters of the substrate, and candidate crystal clusters, which have extreme lattice mismatches, are eliminated. Crystal strains caused by the epitaxial growth are calculated for every candidates of the grown crystal cluster as shown in Table 1. The total energy of grown crystal cluster is estimated by using the total energy as a function of crystal strains. Total energies of candidate crystal clusters are compared with one of the free-strained boundary condition, in order to calculate total energy increments of candidate crystal clusters.

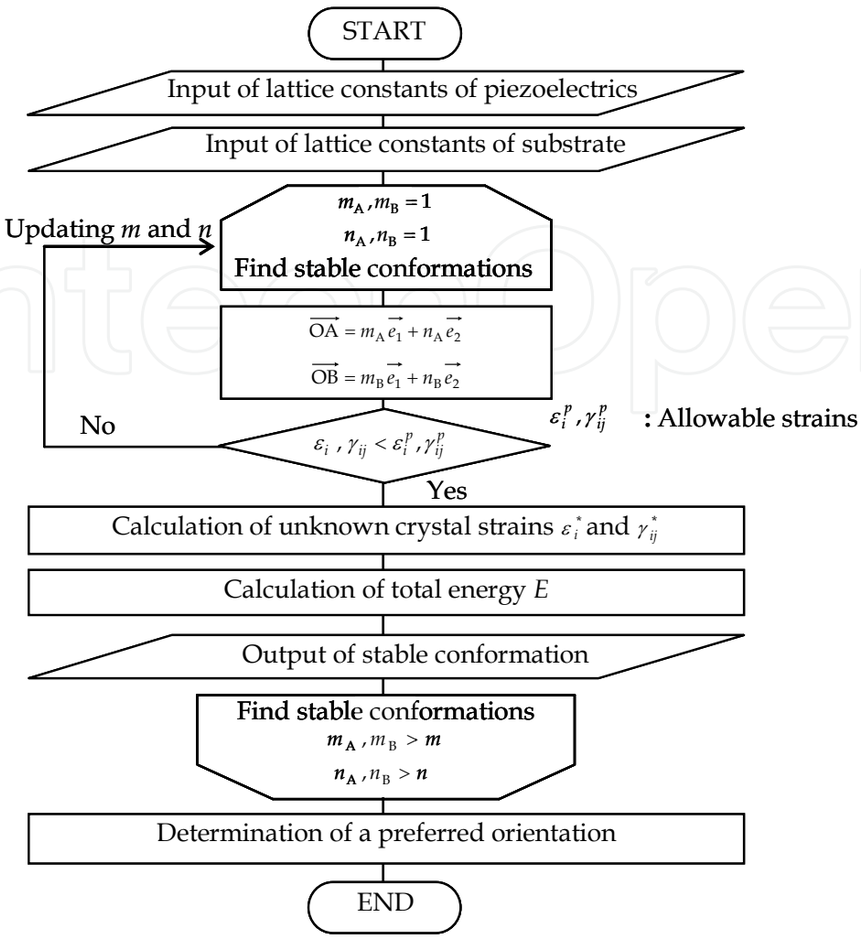


Fig. 5. Flowchart of the process crystallographic simulation.

The fraction of crystal cluster grown on the substrate is calculated by a canonical distribution (Nagaoka et al., 1994).

$$p_i = \frac{\exp\left[-\Delta E_i \,/ k_B T\right]}{\sum_n \exp\left[-\Delta E_n \,/ k_B T\right]} \tag{15}$$

Where ΔE is the total energy increment of the grown cluster, k_B the Boltzmann constant and T the temperature.

2.3 Macro continuum structure analysis by using the crystallographic homogenization method

The crystallographic homogenization method scales up micro heterogeneous structure, such as polycrystalline aggregation, to macro homogeneous structure, such as continuum body. The micro heterogeneous structure has the area Y and microscopic polycrystalline coordinate y, and the macro homogeneous structure has the area X and macroscopic sample coordinate x. Here, it relates to two scales by using the scale ratio λ_h.

$$\lambda_h = \frac{x}{y} \tag{16}$$

where λ_h is an extremely small value. Both coordinates of the micro polycrystalline and the macro continuum structures can be selected independently based on the Eq. (16). Coupling variables are affixed to the superscript λ_h, because the behaviour of the piezo-elastic materials is affected by the polycrystalline structure and λ_h.
The linear piezo-elastic constitutive equation is described as,

$$\sigma_{ij}^{\lambda_h} = C_{ijkl}^{E\lambda_h} \varepsilon_{kl}^{\lambda_h} - e_{kij}^{\lambda_h} E_k^{\lambda_h} \tag{17}$$

$$D_i^{\lambda_h} = e_{ikl}^{\lambda_h} \varepsilon_{kl}^{\lambda_h} + \in_{ik}^{S\lambda_h} E_k^{\lambda_h} \tag{18}$$

The equation of the virtual work of piezoelectric material is written as,

$$\begin{aligned} \int_{\Omega^{\lambda_h}} \left(C_{ijkl}^{E\lambda_h} \varepsilon_{kl}^{\lambda_h} - e_{kij}^{\lambda_h} E_k^{\lambda_h} \right) \frac{\partial \delta u_i^{\lambda_h}}{\partial x_j} \mathrm{d}\Omega + \int_{\Omega^{\lambda}} \left(e_{ikl}^{\lambda_h} \varepsilon_{kl}^{\lambda_h} + \in_{ik}^{S\lambda_h} E_k^{\lambda_h} \right) \frac{\partial \delta \phi^{\lambda_h}}{\partial x_i} \mathrm{d}\Omega \\ = \int_{\Gamma_d^{\lambda}} t_i \, \delta u_i^{\lambda_h} \, \mathrm{d}\Gamma + \int_{\Gamma_e^{\lambda}} \rho \; \delta \phi^{\lambda_h} \, \mathrm{d}\Gamma \end{aligned} \tag{19}$$

where the strain tensor and the electric field tensor are

$$\varepsilon_{ij}^{\lambda_h} = \frac{1}{2}\left(\frac{\partial u_i^0(x)}{\partial x_j} + \frac{\partial u_j^0(x)}{\partial x_i} \right) + \frac{1}{2}\left(\frac{\partial u_i^1(x,y)}{\partial y_j} + \frac{\partial u_j^1(x,y)}{\partial y_i} \right) \tag{20}$$

$$E_i^{\lambda_h} = -\frac{\partial \phi^0(x)}{\partial x_i} - \frac{\partial \phi^1(x,y)}{\partial y_i} \tag{21}$$

It is assumed that the microscopic displacement and the electrostatic potential can be written as the separation of variables:

$$u_i^1(\mathbf{x},\mathbf{y}) = \chi_i^{kl}(\mathbf{x},\mathbf{y}) \frac{\partial u_k^0(\mathbf{x})}{\partial x_l} + \Phi_i^m(\mathbf{x},\mathbf{y}) \frac{\partial \phi^0(\mathbf{x})}{\partial x_m} \tag{22}$$

$$\phi^1(\mathbf{x},\mathbf{y}) = \varphi^{ij}(\mathbf{x},\mathbf{y}) \frac{\partial u_i^0(\mathbf{x})}{\partial x_j} + R^k(\mathbf{x},\mathbf{y}) \frac{\partial \phi^0(\mathbf{x})}{\partial x_k} \tag{23}$$

where $\chi_i^{kl}(x,y)$ is the characteristic displacement of a unit cell, $R^k(x,y)$ the characteristic electrical potential of a unit cell and $\phi^{ij}(x,y)$ and $\Phi_i^m(x,y)$ the characteristic coupling functions of a unit cell. The macroscopic dominant equations are described as,

$$\begin{aligned} \int_Y \left(C_{ijkl}^E \frac{\partial \chi_k^{mn}(x,y)}{\partial y_l} + e_{kij} \frac{\partial \varphi^{mn}(x,y)}{\partial y_k} \right) \frac{\partial \delta u_i^1(x,y)}{\partial y_j} \mathrm{d}Y \\ = -\int_Y C_{ijmn}^E \frac{\partial \delta u_i^1(x,y)}{\partial y_j} \mathrm{d}Y \end{aligned} \tag{24}$$

$$\int_Y \left(e_{ikl} \frac{\partial \chi_k^{mn}(x,y)}{\partial y_l} - \epsilon_{ik}^S \frac{\partial \varphi^{mn}(x,y)}{\partial y_k} \right) \frac{\partial \delta\phi^1(x,y)}{\partial y_i} \mathrm{d}Y = -\int_Y e_{imn} \frac{\partial \delta\phi^1(x,y)}{\partial y_i} \mathrm{d}Y \tag{25}$$

$$\int_Y \left(C_{ijkl}^E \frac{\partial \Phi_k^p(x,y)}{\partial y_l} + e_{kij} \frac{\partial R^P(x,y)}{\partial y_k} \right) \frac{\partial \delta u_i^1(x,y)}{\partial y_j} \mathrm{d}Y = -\int_Y e_{pij} \frac{\partial \delta u_i^1(x,y)}{\partial y_j} \mathrm{d}Y \tag{26}$$

$$\int_Y \left(e_{ikl} \frac{\partial \Phi_k^p(x,y)}{\partial y_l} - \epsilon_{ik}^S \frac{\partial R^P(x,y)}{\partial y_k} \right) \frac{\partial \delta\phi^1(x,y)}{\partial y_i} \mathrm{d}Y = \int_Y \epsilon_{ip}^S \frac{\partial \delta\phi^1(x,y)}{\partial y_i} \mathrm{d}Y \tag{27}$$

where, C_{ijkl}^E is the elastic stiffness tensor at constant electric field, ϵ_{ik}^S the dielectric constant tensor at constant strain and e_{kij} the piezoelectric stress constant tensor. They are calculated by experimentally measured crystal properties. Equations (24) - (27) have the solution under the condition of the periodic boundary. The homogenized elastic stiffness tensor, piezoelectric stress constant tensor and dielectric constant tensor are described by the following characteristic function tensor.

$$C_{ijmn}^{EH} = \frac{1}{|Y|} \int_Y \left(C_{ijmn}^E + C_{ijkl}^E \frac{\partial \chi_k^{mn}(x,y)}{\partial y_l} + e_{kij} \frac{\partial \varphi^{mn}(x,y)}{\partial y_k} \right) \mathrm{d}Y \tag{28}$$

$$\begin{aligned} e_{pij}^H &= \frac{1}{|Y|} \int_Y \left(e_{pij} + e_{kij} \frac{\partial R^P(x,y)}{\partial y_k} + C_{ijkl}^E \frac{\partial \Phi_k^p(x,y)}{\partial y_l} \right) \mathrm{d}Y \\ &= \frac{1}{|Y|} \int_Y \left(e_{pij} + e_{pkl} \frac{\partial \chi_k^{ij}(x,y)}{\partial y_l} - \epsilon_{pk}^S \frac{\partial \varphi^{ij}(x,y)}{\partial y_k} \right) \mathrm{d}Y \end{aligned} \tag{29}$$

$$\epsilon_{ip}^{SH} = \frac{1}{|Y|} \int_Y \left(\epsilon_{ip}^S + \epsilon_{ik}^S \frac{\partial R^P(x,y)}{\partial y_k} - e_{ikl} \frac{\partial \Phi_k^p(x,y)}{\partial y_l} \right) \mathrm{d}Y \tag{30}$$

where superscript *H* means the homogenized value.

The conventional two-scale finite element analysis is based on the crystallographic homogenization method. In this conventional analysis, the virtually determined or experimentally measured orientations are employed for the micro crystalline structure to characterize the macro homogenized piezoelectric properties. However, this conventional analysis can not characterize a new piezoelectric thin film because of unknown crystal structure and material properties.

A newly proposed three-scale structure analysis can scale up and characterize the crystal structure to the micro polycrystalline and macro continuum structures. First, the stable structure and properties of the new piezoelectric crystal are evaluated by using the first-principles DFT. Second, the crystal growth process of the new piezoelectric thin film is analyzed by using the process crystallographic simulation. The preferred orientation and their fractions of the micro polycrystalline structure are predicted by this simulation. Finally, the homogenized piezoelectric properties of the macro continuum structure are characterized by using the crystallographic homogenization theory. Comparing the provability of crystal growth and the homogenized piezoelectric properties of the new piezoelectric thin film on several substrates, the best substrate is found by using the three-scale structure analysis. It is confirmed that the three-scale structure analysis can design not only existing thin films but also new piezoelectric thin films.

3. Three-scale structure analysis of a new biocompatible piezoelectric thin film

3.1 Crystal structure analysis by using the first-principles calculation

The biocompatible elements (Ca, Cr, Cu, Fe, Ge, Mg, Mn, Mo, Na, Ni, Sn, V, Zn, Si, Ta, Ti, Zr Li, Ba, K, Au, Rb, In) were assigned to A cation in the perovskite-type compound ABO_3. Silicon, which was one of well-known biocompatible elements, was employed on B cation. Values of tolerance factor were calculated by using Pauling's ionic radius. Five silicon oxides satisfied the geometrical compatibility condition, where $MgSiO_3$ = 0.88, $MnSiO_3$ = 0.93, $FeSiO_3$ = 0.91, $ZnSiO_3$ = 0.91 and $CaSiO_3$ = 1.01.

The stable cubic structure with minimum total energy was calculated for the five silicon oxides. As the cubic structure has a feature of high symmetry, the stable crystal structure was easy to estimate because of a little dependency on the initial atomic coordinates. Table 2 shows the lattice constants of the silicon oxide obtained by the first-principles DFT.

The phonon properties of cubic structure at paraelectric non-polar phase were calculated to consider phase transition to other crystal structures. Table 3 summarizes the eigenfrequency, the phonon vibration mode and the eigenvector components normalized to unity. $MgSiO_3$, $MnSiO_3$, $FeSiO_3$, $ZnSiO_3$ showed negative values of eigenfrequency. Cubic structures of these four silicon oxides became unstable owing to softening atomic vibration, and they had possibility of the phase transition to other crystal structure. On the other hand, the stable structure of $CaSiO_3$ was the cubic structure due to positive value of eigenfrequency.

The phonon vibration modes are also summarized in Table 3. All eigenvectors of $MgSiO_3$, $MnSiO_3$ and $FeSiO_3$ were almost parallel to *c* axis in crystallographic coordinate system. These three silicon oxides had a high possibility to change from the cubic structure to the tetragonal structure, which showed superior piezoelectricity. The eigenvector of O_I and O_{II} in $ZnSiO_3$, however, included a component perpendicular to *c* axis. It was expected that $ZnSiO_3$ changed from cubic structure to other structures consisting of a rotated SiO_6–octahedron, such as the orthorhombic structure with inferior piezoelectricity.

The stable tetragonal structure to minimize the total energy was calculated for the above three silicon oxides, $MgSiO_3$, $MnSiO_3$ and $FeSiO_3$. Total energies of these tetragonal structures were lower than those of the stable cubic structure. Table 4 shows lattice constants and internal coordinates of constituent atoms. In comparison of the aspect ratio among the three silicon oxides, the value of $MgSiO_3$ was larger than 1.0. On the other hand,

the aspect ratio of $MnSiO_3$ and $FeSiO_3$ were smaller than 1.0. Generally, the tetragonal structure of typical perovskite-type oxides such as $BaTiO_3$ and $PbTiO_3$ had larger aspect ratio than 1.0. Consequently, the tetragonal structure of $MnSiO_3$ and $FeSiO_3$ could not be existed. The above results have indicated that $MgSiO_3$ was a remarkable candidate for the new biocompatible piezoelectric material.

Material	Lattice constant (nm)
$MgSiO_3$	0.3459
$MnSiO_3$	0.3431
$FeSiO_3$	0.3421
$ZnSiO_3$	0.3454
$CaSiO_3$	0.3520

Table 2. The lattice constants of cubic structure for candidates of the piezoelectric material.

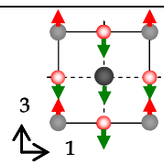
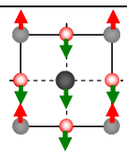
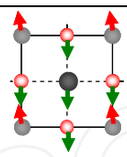
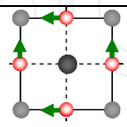
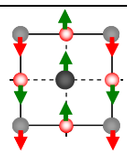
Material	Eigenfrequency (cm^{-1})	Phonon eigenvector				
		Mode	components			
			Atom	ξ_1	ξ_2	ξ_3
$MgSiO_3$	-112		O_I	0.00	0.00	-0.37
			O_{II}	0.00	0.00	-0.37
			O_{III}	0.00	0.00	-0.22
			Si	0.00	0.00	-0.13
			Mg	0.00	0.00	0.88
$MnSiO_3$	-41		O_I	-0.09	0.00	-0.53
			O_{II}	-0.07	0.00	-0.53
			O_{III}	-0.09	0.00	-0.41
			Si	-0.07	0.00	-0.45
			Mn	0.04	0.00	0.23
$FeSiO_3$	-83		O_I	0.08	0.01	-0.32
			O_{II}	0.04	0.00	-0.32
			O_{III}	0.08	0.00	-0.17
			Si	0.03	0.00	-0.13
			Fe	-0.22	-0.02	0.83
$ZnSiO_3$	-267		O_I	0.24	0.00	-0.66
			O_{II}	0.00	-0.05	0.66
			O_{III}	-0.24	0.05	0.00
			Si	0.00	0.00	0.00
			Zn	0.00	0.00	0.00
$CaSiO_3$	238		O_I	0.00	0.00	-0.35
			O_{II}	0.01	0.00	-0.35
			O_{III}	0.01	0.00	0.29
			Si	-0.01	0.00	0.79
			Ca	0.00	0.00	-0.23

Table 3. Comparison of phonon properties of cubic structure among $MgSiO_3$, $MnSiO_3$, $FeSiO_3$, $ZnSiO_3$ and $CaSiO_3$.

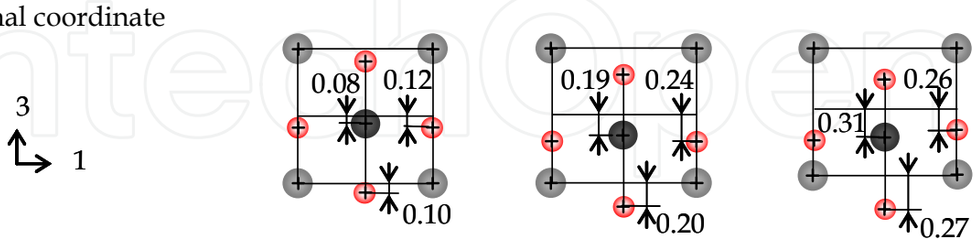
	$MgSiO_3$	$MnSiO_3$	$FeSiO_3$
Lattice constant	$a = b = 0.3449$	$a = b = 0.3547$	$a = b = 0.3602$
(nm)	$c = 0.3538$	$c = 0.3440$	$c = 0.3349$
Aspect ratio	1.026	0.970	0.930
Internal coordinate			

Table 4. Lattice constants and internal coordinates of constituent atoms for tetragonal structure of $MgSiO_3$, $MnSiO_3$ and $FeSiO_3$.

	Mg	Si	O_I	O_{II}	O_{III}
Z^*_{11}	2.331	3.995	-3.024	-1.620	-1.682
Z^*_{22}	2.331	3.995	-1.620	-3.024	-1.682
Z^*_{33}	2.254	4.054	-1.637	-1.637	-3.035

Table 5. Born effective charge in tetragonal structure of $MgSiO_3$ perovskite.

		$MgSiO_3$	$BaTiO_3$	
			DFT	Experiment
Spontaneous polarization (C/m^2)	P_3^S	0.471	0.226	0.260
Piezoelectric stress constant (C/m^2)	e_{33}	4.57	6.11	3.66
	e_{31}	-2.20	-3.49	-2.69
	e_{15}	12.77	21.34	21.30

Table 6. Comparison of the spontaneous polarization and piezoelectric stress constant between $MgSiO_3$ and $BaTiO_3$.

Table 5 shows Born effective charges of each atoms of $MgSiO_3$. Piezoelectric properties, including the spontaneous polarization and piezoelectric stress constants e_{31}, e_{33} and e_{15}, were calculated by these Born effective charges. Table 6 summarizes piezoelectric properties of $MgSiO_3$, those of $BaTiO_3$ calculated by the DFT and observed by the experiment. It could be concluded that $MgSiO_3$ had larger spontaneous polarization than one of $BaTiO_3$. $MgSiO_3$ showed good piezoelectric properties, which were e_{33} = 4.57 C/m^2, e_{31} = -2.20 C/m^2 and e_{15} = 12.77 C/m^2.

3.2 Investigation of the best substrate of the biocompatible piezoelectric material $MgSiO_3$

Three biocompatible atoms, which include Au, Mo and Fe, were selected for the substrate candidate. This is because;

1. these atoms can be used for the under electrode.
2. chemical elements of these atoms have the cubic crystal structure.

Lattice constants of Au with FCC cubic structure are $a = b = c = 0.4080$ nm, and ones of Mo with BCC cubic structure are $a = b = c = 0.3147$ nm. Ones of Fe with BCC cubic structure are $a = b = c = 0.2690$ nm.

Crystal growth process of $MgSiO_3$ thin film on (100) and (111) facets of candidate substrates were demonstrated by using the process crystallographic simulation. Tables 7 - 9 show numerical results of $MgSiO_3$ thin film grown on (100) facets of these four substrates, and Tables 10 - 12 show results of one on (111) facets of the substrates.

Table 13 shows summary of the orientation fractions of $MgSiO_3$ thin film on substrates calculated by canonical distribution. In the case of Mo(100) substrate as shown in Table 8, $MgSiO_3$[100] and [001] were grown, and their orientation fraction were 61.5 % and 38.5 %, respectively. $MgSiO_3$[001] was grown on Au(100) and Fe(100) at 100 % probability. Comparing total energy increments of crystal clusters of $MgSiO_3$ grown on these substrates, $MgSiO_3$[001] on Fe(100) substrate was more stable due to the lowest total energy increment as shown in Table 9. $MgSiO_3$[111] was grown on Au(111) and Mo(111) substrates at 100 % provability.

Orientation	[001]	[001]	[001]
ε_a (%)	0.21	0.48	0.64
ε_b (%)	0.21	0.48	0.64
ε_c (%)	0.00	0.00	0.00
γ_{ab} (%)	0.00	0.00	0.00
γ_{bc} (%)	0.00	0.00	0.00
γ_{ca} (%)	0.00	0.00	0.00
Total energy of the unit cell (eV)	-2398.4025	-2398.3984	-2398.3946
Total energy increment (eV)	0.0749	0.1257	0.3158

Table 7. Analytical results for stable conformations and preferred orientations of $MgSiO_3$ thin film grown on Au(100) substrate.

Orientation	[100]	[001]	[001]
ε_a (%)	0.00	1.13	-0.50
ε_b (%)	1.13	1.13	-0.50
ε_c (%)	-1.41	-0.50	0.00
γ_{ab} (%)	0.00	0.00	0.00
γ_{bc} (%)	0.00	-0.50	0.00
γ_{ca} (%)	0.00	0.00	0.00
Total energy of the unit cell (eV)	-2398.3803	-2398.3772	-2398.3979
Total energy increment (eV)	0.0925	0.1046	0.4447

Table 8. Analytical results for stable conformations and preferred orientations of $MgSiO_3$ thin film grown on Mo(100) substrate.

Comparing total energy increments of crystal clusters of $MgSiO_3$ grown on these two substrates, Au(111) was better substrate than Mo(111) due to low total energy increment. $MgSiO_3$[111] and [001] on Fe(111) were grown at 97.8 % and 2.2 % probability, respectively. Consequently, it could be concluded that four substrates, which included Mo(100), Fe(100) and (111), Au(111), were candidates of the best substrate for $MgSiO_3$ thin film.

Orientation	[001]	[001]	[001]
ε_a (%)	-0.11	0.29	-0.56
ε_b (%)	-0.11	0.29	-0.56
ε_c (%)	0.00	0.00	0.00
γ_{ab} (%)	0.00	0.00	0.00
γ_{bc} (%)	0.00	0.00	0.00
γ_{ca} (%)	0.00	0.00	0.00
Total energy of the unit cell (eV)	-2398.4032	-2398.4016	-2398.3966
Total energy increment (eV)	0.0060	0.0906	0.1092

Table 9. Analytical results for stable conformations and preferred orientations of $MgSiO_3$ thin film grown on Fe(100) substrate.

Orientation	[111]	[001]	[111]
ε_a (%)	2.55	0.06	1.50
ε_b (%)	2.55	0.06	1.50
ε_c (%)	-0.03	0.00	-1.05
γ_{ab} (%)	-0.50	2.20	0.00
γ_{bc} (%)	-0.50	0.00	0.00
γ_{ca} (%)	-0.50	0.00	2.20
Total energy of the unit cell (eV)	-2398.2686	-2398.3450	-2398.3546
Total energy increment (eV)	0.5393	2.1038	2.3891

Table 10. Analytical results for stable conformations and preferred orientations of $MgSiO_3$ thin film grown on Au(111) substrate.

Orientation	[111]	[111]	[001]
ε_a (%)	0.73	0.93	-0.50
ε_b (%)	0.73	0.93	-1.53
ε_c (%)	-1.81	-1.61	0.50
γ_{ab} (%)	0.00	0.00	0.00
γ_{bc} (%)	0.00	0.00	0.50
γ_{ca} (%)	0.00	0.00	0.00
Total energy of the unit cell (eV)	-2398.3724	-2398.3717	-2398.3796
Total energy increment (eV)	0.7738	1.5518	1.9276

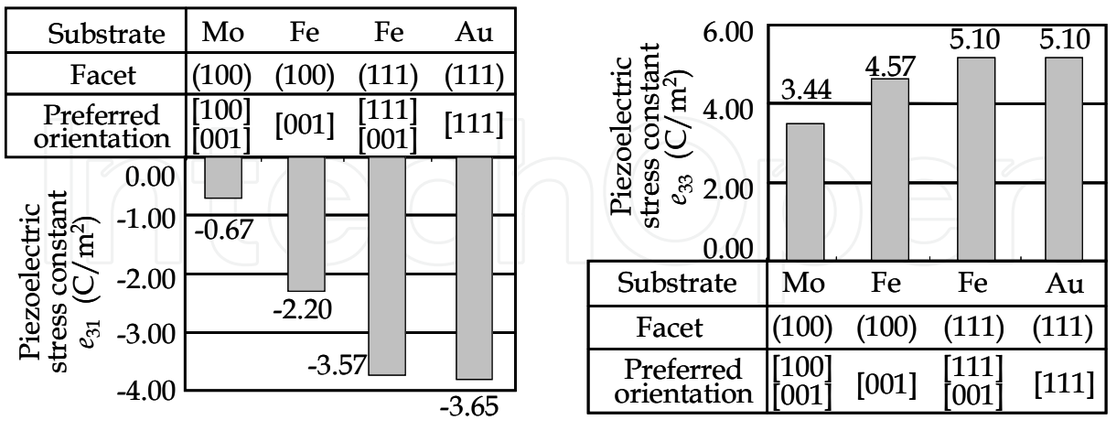
Table 11. Analytical results for stable conformations and preferred orientations of $MgSiO_3$ thin film grown on Mo(111) substrate.

Orientation	[111]	[001]	[111]
ε_a (%)	1.33	-0.56	3.19
ε_b (%)	1.33	-0.56	3.19
ε_c (%)	-1.22	0.50	0.60
γ_{ab} (%)	0.00	2.20	-0.50
γ_{bc} (%)	0.00	0.50	-0.50
γ_{ca} (%)	0.00	0.00	-0.50
Total energy of the unit cell (eV)	-2398.3618	-2398.3557	-2398.1793
Total energy increment (eV)	0.6661	0.7639	0.8962

Table 12. Analytical results for stable conformations and preferred orientations of $MgSiO_3$ thin film grown on Fe(111) substrate.

Substrate Atom	Facet	$MgSiO_3$ Orientation	Fraction (%)
Au	(100)	[001]	100.0
	(111)	[111]	100.0
Mo	(100)	[100]	61.5
		[001]	38.5
	(111)	[111]	100.0
Fe	(100)	[001]	100.0
	(111)	[111]	97.8
		[001]	2.2

Table 13. Analytical results of preferred orientations and their fractions for $MgSiO_3$ thin films grown on various substrates.



(a) Piezoelectric stress constant e_{31} (b) Piezoelectric stress constant e_{33}

Fig. 6. Homogenized piezoelectric stress constant of $MgSiO_3$ thin film on various substrates.

Analytically determined piezoelectric stress constants and orientation fractions of $MgSiO_3$ were introduced into the macro continuum structure analysis. Homogenized piezoelectric strain constants of the $MgSiO_3$ thin film on four substrate candidates were calculated.

Figure 6(a) shows homogenized e_{31} constants and Fig. 6(b) e_{33}. Substrates, facets of substrates and orientation fractions of $MgSiO_3$ thin film were also shown in figures. $MgSiO_3$[111] on Au(111) substrate indicated the highest piezoelectric stress constants, e_{31} = -3.65 C/m² and e_{33} = 5.10 C/m². $MgSiO_3$[001] on Fe(100) showed e_{31} = -2.20 C/m² and e_{33} = 4.57 C/m². e_{31} of $MgSiO_3$[001] on Fe(100) was 39.7 % lower than one on Au(111) and e_{33} of $MgSiO_3$[001] on Fe(100) was 10.4 % lower than one on Au(111). In the case of Fe(111) substrate, e_{33} was equal to one on Au(111) substrate, however e_{31} was smaller than one on Au(111). Furthermore, $MgSiO_3$ on Au(111) was more stable than one on Fe(111) substrate. These results have concluded that Au(111) was the best substrate for $MgSiO_3$ thin film.

4. A new biocompatible piezoelectric $MgSiO_3$ thin film generation

4.1 Experimental method

$MgSiO_3$ tihn film is generated by radio-frequency magnetron sputtering. Three factors are selected for generating perovskite tetragonal structure and high piezoelectric property. These conditions are i) the substrate temperature T_s, ii) the post-annealing temperature T_a and iii) flow rate of oxygen f_{O2}. This is because that i) the substrate temperature contributes configuration and bonding of thin film crystals, and ii) the post-annealing temperature affects crystallization of amorphous crystal. iii) The flow rate of oxygen affects crystal morphology and composition of the $MgSiO_3$ crystal. These generation conditions are set as T_a = 300 °C, 350 °C, 400 °C, T_s = 600 °C, 650 °C, 700 °C, and f_{O2} = 1.0 sccm, 3.0 sccm, 5.0 sccm, respectively. The target material is used the mixed sinter of MgO and SiO_2, the substrate is Au(111)/$SrTiO_3$(110), which is determined by the three-scale structure analysis. The electric power is 100 W, flow rate of Ar gas is 10 sccm and the pressure in chamber during the sputtering is 0.5 Pa. Thin film is sputtered 4 hours and post-annealed an hour after sputtering.

The displacement–voltage curve of $MgSiO_3$ thin film is measured by ferroelectric character evaluation (FCE) system. Generally, displacement-voltage curve of the piezoelectric material shows butterfly-type hysteresis curve. The piezoelectric strain constant d_{33} can be calculated by gradient of the butterfly-type hysteresis curve. The response surface methodology (RSM) (Berger & Maurer, 2002) is employed to find the optimum combination of generation factor levels of the $MgSiO_3$ thin film.

4.2 Generation of the new biocompatible piezoelectric $MgSiO_3$ thin film

Displacement-voltage curves under the conditions of f_{O2} = 1.0, 3.0 and 5.0 sccm are shown in Fig. 7 - 9. All thin films showed the piezoelectric property due to butterfly-type hysteresis curves. The piezoelectric strain constant d_{33} could be calculated by the gradient at cross point of the butterfly-type hysteresis curve, and d_{33} was indicated in all graphs. d_{33} constants of all thin films were larger than the d_{33} constant (= 129.4 pm/V) of $BaTiO_3$, which was commonly used lead-free piezoelectric material generated in our previous study.

The optimum conditions for generating the $MgSiO_3$ thin film were found by using RSM. Figure 10 shows the response surface of d_{33} constant as a function of T_s and T_a under the condition of f_{O2}= 4.0 sccm. Figure 10(a) shows the aerial view and Fig. 10(b) top view. The black point indicates the highest point of d_{33} constant. The optimum condition, for T_s= 300 °C, T_a= 631 °C and f_{O2}= 4.0 sccm, was found.

$MgSiO_3$ thin film was generated at T_s = 250 °C, because the obtained best T_s was lowest temperature in the range of the substrate temperature which was set in this study. However, the displacement-voltage curves were not indicated the butterfly-type hysteresis curve. This is because the thin film was not crystallized to $MgSiO_3$, due to inactive adatoms and low collision rate of adatoms.

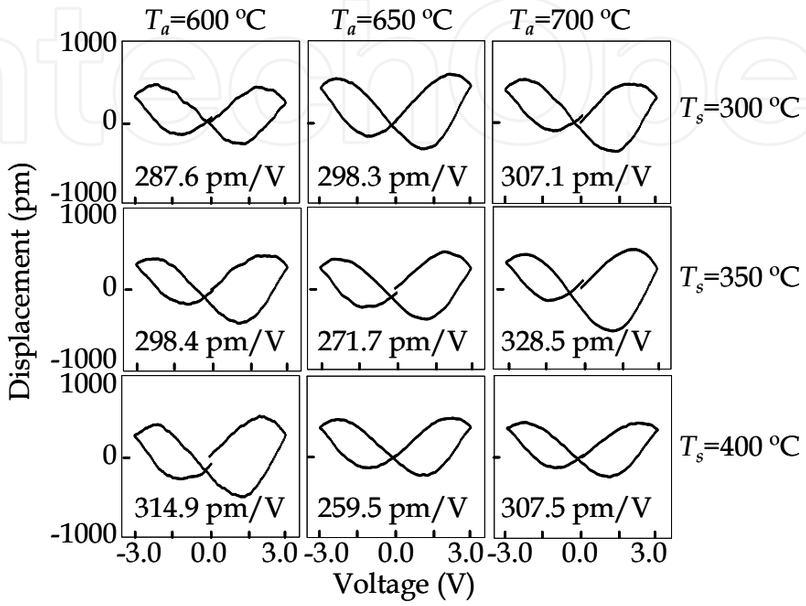


Fig. 7. Displacement-voltage curves of $MgSiO_3$ thin films in the case of f_{O2} = 1.0 sccm.

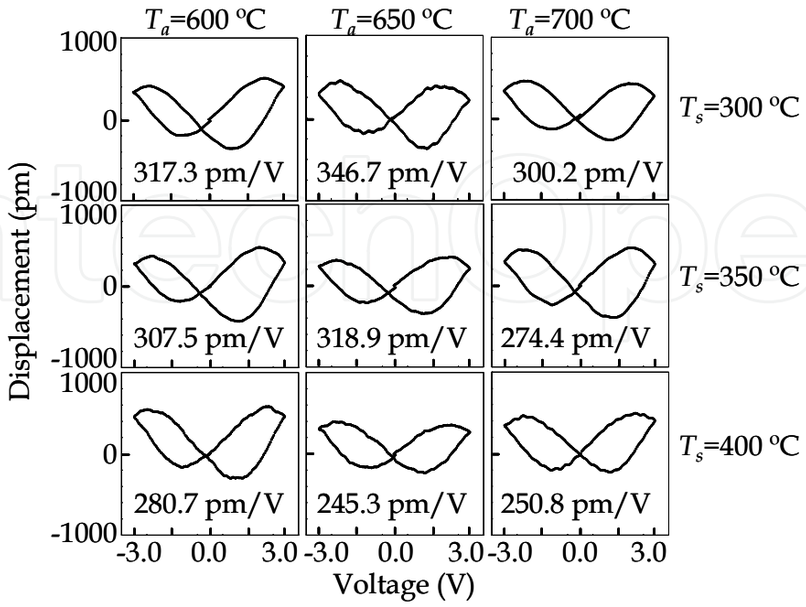


Fig. 8. Displacement-voltage curves of $MgSiO_3$ thin films in the case of f_{O2} = 3.0 sccm.

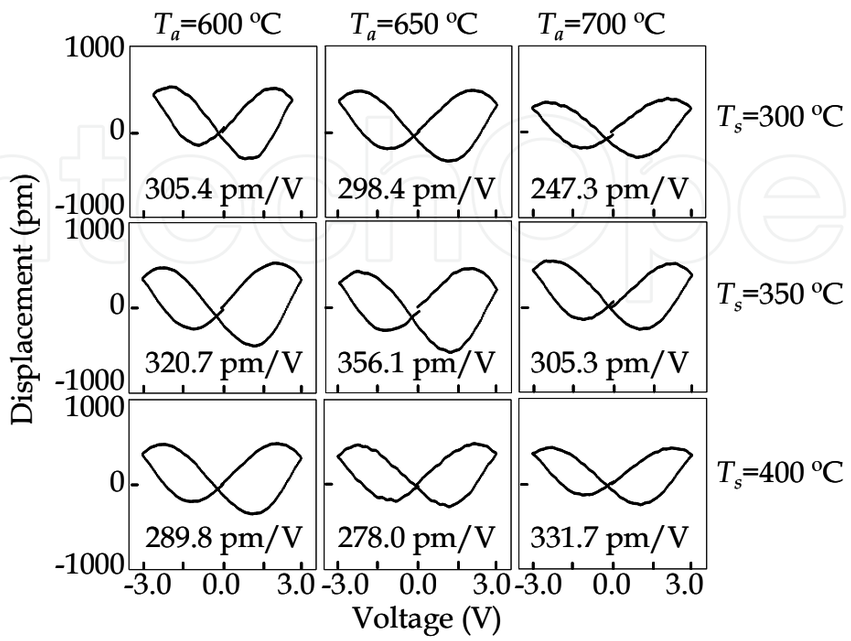


Fig. 9. Displacement-voltage curves of $MgSiO_3$ thin films in the case of f_{O2} = 5.0 sccm.

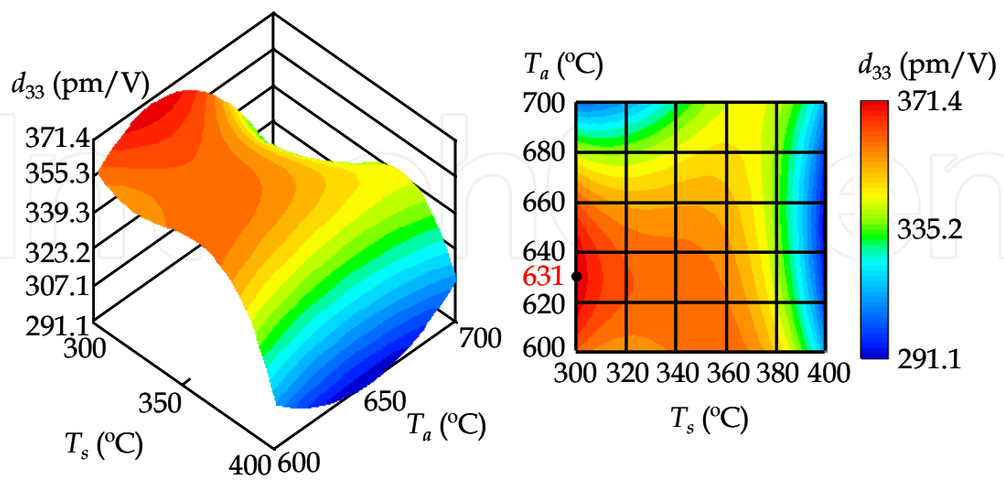


Fig. 10. Piezoelectric strain constant d_{33} as functions of T_s and T_a in the case of f_{O2} = 4.0sccm.

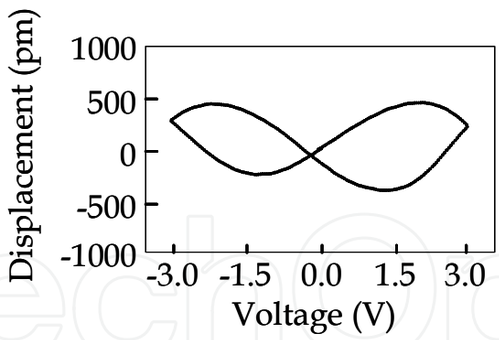


Fig. 11. Displacement-voltage curve of $MgSiO_3$thin film generated at the optimum condition, T_s = 300 °C, T_a = 631 °C and f_{O2} = 4.0 sccm.

Finally, $MgSiO_3$ thin film was generated at the optimum condition. Figure 11 shows its displacement-voltage curve. d_{33} constant was obtained as 359.2 pm/V and this value was higher than one of the pure PZT thin films, d_{33} = 307.0 pm/V, generated by Z. Zhu et al (Zhu et al, 2010).
Consequently, the piezoelectric $MgSiO_3$ thin film was generated successfully and it can be used for sensors and actuators for MEMS or NENS.

5. Conclusion

In this study, the three-scale structure analysis code, which is based on the first-principles density functional theory (DFT), the process crystallographic simulation and the crystallographic homogenization theory, was newly developed. Consequently, a new biocompatible $MgSiO_3$ piezoelectric material was generated by using the radio-frequency (RF) magnetron sputtering system, where its optimum generating condition has been found analytically and experimentally.
Section 2 discussed the algorithm of the three-scale structure analysis, which can design epitaxially grown piezoelectric thin films. This analysis was constructed in three-scale structures, such as a crystal structure, a micro polycrystalline structure and a macro continuum structure. The existing two-scale analysis could evaluate the property of the macro continuum structure by using experimentally observed information of crystal structure, such as crystallographic orientation and properties of the crystal. The three-scale structure analysis can design new biocompatible piezoelectric thin films through three steps, which were to calculate the crystal structure by using the first-principles DFT, to evaluate the epitaxial growth process by using crystallographic simulation, and to calculate the homogenized properties of thin film by using the crystallographic homogenization theory.
In section 3, in order to find a new biocompatible piezoelectric crystal and its best substrate, the three-scale structure analysis was applied to the silicon oxides. Consequently, $MgSiO_3$ had a large spontaneous polarization $P_3^S = 0.471\ \mathrm{C/m^2}$ and it could present good piezoelectric stress constants e_{33} = 4.57 C/m², e_{31} = -2.20 C/m² and e_{15} = 12.77 C/m². These results indicated that $MgSiO_3$ was one of the candidates of the new biocompatible piezoelectric thin film. Au(111) was the best substrate of $MgSiO_3$ thin film, because $MgSiO_3$[111] on Au(111) was most stable and showed highest piezoelectric stress constant e_{31}= -3.65 C/m² and e_{33}= 5.10 C/m².

In section 4, $MgSiO_3$ piezoelectric thin film was generated by using the RF magnetron sputtering system. The optimum condition was found by using the response surface methodology (RSM). Measuring the piezoelectric properties of the thin films by using the ferroelectric character evaluation (FCE) system, all $MgSiO_3$ thin films showed the piezoelectric property due to butterfly-type hysteresis curves. Finally, the optimum condition for T_s = 300 ºC, T_a = 631 ºC and f_{O2} = 4.0 sccm, was found and the best piezoelectric strain constant d_{33} = 359.2 pm/V was obtained. This value was higher than the one of the pure PZT thin films, d_{33}= 307.0 pm/V, generated by Z. Zhu et al.. Consequently, the piezoelectric $MgSiO_3$ thin film was generated successfully and it can be used for sensors and actuators for MEMS or NENS.

6. References

Hindrichsena, C., Møllerb, R., Hansenc, K. & Thomsena, E. (2010). Advantages of PZT Thick Film for MEMS Sensors, *Sensors and Actuators A: Physical*, (Oct. 2009) pp. 1-6, 0924-4247.

Koh, K., Kobayashi, T., Hsiao, F. & Lee, C. (2010). Characterization of Piezoelectric PZT Beam Actuators for Driving 2D Scanning Micromirrors, *Sensors and Actuators A: Physical*, (Sep, 2009), pp.1-12, 0924-4247.

Zhang, M., Jia, Z. & Ren, T. (2009). Effects of Electrodes on the Properties of Sol-Gel PZT Based Capacitors in FeRAM, *Solid-State Electronics*, Vol.53, (Aug. 2008), pp.473-477, 0038-1101.

Ma, Y., Kong, F., Pan, C., Zhang, Q. & Feng, Z. (2010). Miniature Tubular Centrifugal Piezoelectric Pump Utilizing Wobbling Motion, *Sensors and Actuators A: Physical*, Vol.157, (Jul. 2009), pp.322-327, 0924-4247.

Bose, A., Maity, T., Bysakh, S., Seal, A. and Sen, S. (2010). Influence of Plasma Pressure on the Growth Characteristics and Ferroelectric Properties of Sputter-Deposited PZT Thin Films, *Applied Surface Science*, Vol.256, (Feb. 2010), pp.6205-6212, 0169-4332.

Tohma, T., Masumoto, H. & Goto, T. (2002). Preparation of $BaTiO_3$ Films by Metal-Organic Chemical Vapor Deposition, *Japanese Journal of Applied. Physics Part1*, Vol.41, No.11B, (May 2002), pp.6643-6646, 0021-4922.

Kim, T., Kim, B., Lee, W., Moon, J., Lee, B. & Kim, J. (2006). Integration of Artificial $SrTiO_3$/$BaTiO_3$ Superlattices on Si Substrates using a TiN Buffer Layer by Pulsed Laser Deposition Method, *Journal of Crystal Growth*, Vol.289, No.2, (Aug. 2006), pp.540-546, 0022-0248.

Avrutin, V., Liu, H., Izyumskaya, N., Xiao, B., Ozgur, U. & Morkoc, H. (2009). Growth of $Pb(Ti,Zr)O_3$ Thin Films by Metal-Organic Molecular Beam Epitaxy, *Journal of Crystal Growth*, Vol.311, (Oct. 2008), pp.1333-1339, 0022-0248.

Nishida, K., Wada, S., Okamoto, S., Ueno, R., Funakubo, H. & Katoda, T. (2005). Domain Distributions in Tetragonal $Pb(Zr,Ti)O_3$ Thin Films Probed by Polarized Raman Spectroscopy, *Applied Physics Letters*, Vol.87, (2005), pp.232902.1-232902.3, 0003-6951.

Geetika & Umarji, A. (2010) The Influence of Zr/Ti Content on the Morphotropic Phase Boundary in the PZT–PZN System, *Materials Science and Engineering B*, Vol.167, (Sep. 2009), pp.171-176, 0921-5107.

Kim, K., Hsu, D., Ahn, B., Kim, Y. & Barnard, D. (2010). Fabrication and Comparison of PMN-PT Single Crystal, PZT and PZT-based 1-3 Composite Ultrasonic Transducers for NDE Applications, *Ultrasonics*, Vol.50, (Feb. 2009), pp.790-797, 0041-624X.

Zhu, J., Zheng, L., Luo, W., Li, Y., & Zhang, Y. (2006). Microstructural and Electrical Properties of $BaTiO_3$ Epitaxial Films on $SrTiO_3$ Substructures with a $LaNiO_3$ Conductive Layer as a Template, *Journal of Physic D,* Vol.39. (Feb. 2006), pp.2438-2443, 1361-6463.

Zhang, S., Zhang, H., Zhang, B. & Zhao, G. (2009). Dielectric and Piezoelectric Properties of $(Ba_{0.95}Ca_{0.05})(Ti_{0.08}Zr_{0.12})O_3$ Ceramics Sintered in A Protective Atmosphere, *Journal of European Ceramics Society*, Vol.29, (Apr. 2009), pp.3235-3242, 0955-2219.

Fu, P., Xu, Z., Chu, R., Li, W., Zhang, G. & Hao, J. (2010). Piezoelectric, Ferroelectric and Dielectric Properties of La_2O_3-doped $(Bi_{0.5}Na_{0.5})_{0.94}Ba_{0.06}TiO_3$ Lead-Free Ceramics, *Materials and Design*, Vol.31, (May 2009), pp.796-801, 0261-3069.

Rubio, J., Jaraiz, M., Bragado, I., Mangas, J., Barblla, J. & Gilmer, G. (2003). Atomistic Monte Carlo Simulations of Three-Dimensional Polycrystalline Thin Films, *Journal of Applied Physics*, Vol.94, (Aug. 2002), pp.163-168, 0021-8979.

Lee, S. & Chung, Y. (2006). Surface Characteristics of Epitaxially Grown Ni Layers on Al Surfaces: Molecular Dynamics Simulation, *Journal of Applied Physics*, Vol.100, No.7, (Feb. 2006), pp.074905.1-074905.4, 0021-8979.

Xu, J. & Feng, J. (2002). Study of Ge Epitaxial Growth on Si Substrates by Cluster Beam Deposition, *Journal of Crystal Growth*, Vol.240, No.3 (Jan. 2002), pp.407-404, 0022-0248.

Paul, J., Nishimatsu, T., Kawazoe, Y. & Waghmare, U. (2007). Ferroelectric Phase Transitions in Ultrathin Films of $BaTiO_3$, *Physical Review Letters*, Vol.99, No.7, (Dec. 2005), pp.077601.1-077601.4, 0031-9007.

Costa, S., Pizani, P., Rino, J. & Borges, D. (2006). Structural Phase Transition and Dynamical Properties of $PbTiO_3$ Simulated by Molecular Dynamics, *Journal of Condensed Matter*, Vol.75, No.6, (Sep. 2005), pp.064602.1-064602.5, 0953-8984.

Dieguez, O., Rabe, K. & Vanderbilt, D. (2005). First-Principles Study of Epitaxial Strain in Perovskites, *Physical Review B*, Vol.72, No.14, (Jun. 2005), pp.144101.1-144101.9, 1098-0121.

Yakovkin, I. & Gutowski, M. (2004). $SrTiO_3$/Si(001) Epitaxial Interface: A Density Functional Theory Study, *Physical Review B*, Vol.70, No.16, (Nov. 2003), pp.165319.1-165319.7, 1098-0121.

Jayachandran, K., Guedes, J. & Rodrigues, H. (2009). Homogenization of Textured as well as Randomly Oriented Ferroelectric Polycrystals, *Computational Materials Science*, Vol.45, (Nov. 2007), pp.816-820, 0927-0256.

Segall, M., Lindan, P., Probert, M., Pickard, C., Hasinp, P., Clark, S. & Payne, M. (2002). First-Principles Simulation: Ideas, Illustrations and the CASTEP Code, *Journal of Physics: Condensed Matter*, Vol.14, (Jan. 2002), pp.2717-2744, 0953-8984.

Monkhorst, H. & Pack, J. (1976). Special Points for Brilloun-Zone Integrations, *Physical Review B*, Vol.13, No.12, (Jan. 1976), pp.5188-5192, 1098-0121.

Szabo, G., Choen, R. & Krakauer, H. (1998). First-Principles Study of Piezoelectricity in $PbTiO_3$, *Physical Review Letters*, Vol.80, No.19, (Oct. 1997), pp.4321-4324, 0031-9007.

Szabo, G., Choen, R. & Krakauer, H. (1999). First-Principles Study of Piezoelectricity in Tetragonal $PbTiO_3$ and $PbZr_{1/2}Ti_{1/2}O_3$, *Physical Review B*, Vol.59, No.20, (Sep. 1998), pp.12771-12776, 1098-0121.

King-Smith, R. & Vanderbilt, D. (1993). Theory of Polarization of Crystalline Solids, *Physical Review B*, Vol.47, No.3, (Jun. 1992), pp.1651-1654, 1098-0121.

Olsson, A. & Sandberg, G. (2002). Latin Hypercube Sampling for Stochastic Finite Element Analysis, *Journal of Engineering Mechanics*, Vol.128, No.1, (Sep. 1999), pp.121-125, 0733-9399.

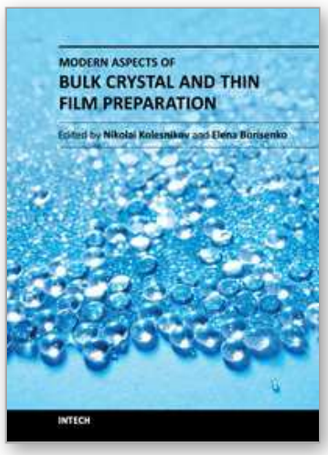
Sakata, S., Ashida, F. & Zako, M. (2007). Hybrid Approximation Algorithm with Kriging and Quadratic Polynomial-based Approach for Approximate Optimization, *International Journal for Numerical Methods in Engineering*, Vol.70, No.6, (Jul. 2005), pp.631-654, 1097-0207.

Nagaoka, Y. (6th Jul. 1994). *Statistical Mechanics* (in Japanese), Iwanami Shoten, 4-000-07927-1, Japan, Tokyo.

Berger, P. & Maurer, R. (2002). *Experimental Design*, Duxbury Thomson Learning Inc, 0-534-35822-5, USA, Calfornia.

Zhu, Z., Li, J., Liu, Y. & Li, J. (2009). Shifting of the Morphotropic Phase Boundary and Superior Piezoelectric Response in Nb-doped Pb(Zr, Ti)O_3 Epitaxial Thin Films, *Acta Materialia*, Vol.57, (Feb. 2009), pp.4288-4295, 1359-6454.

IntechOpen



Modern Aspects of Bulk Crystal and Thin Film Preparation

Edited by Dr. Nikolai Kolesnikov

ISBN 978-953-307-610-2
Hard cover, 608 pages
Publisher InTech
Published online 13, January, 2012
Published in print edition January, 2012

In modern research and development, materials manufacturing crystal growth is known as a way to solve a wide range of technological tasks in the fabrication of materials with preset properties. This book allows a reader to gain insight into selected aspects of the field, including growth of bulk inorganic crystals, preparation of thin films, low-dimensional structures, crystallization of proteins, and other organic compounds.

How to reference

In order to correctly reference this scholarly work, feel free to copy and paste the following:

Hwisim Hwang, Yasutomo Uetsuji and Eiji Nakamachi (2012). Three-Scale Structure Analysis Code and Thin Film Generation of a New Biocompatible Piezoelectric Material MgSiO3, Modern Aspects of Bulk Crystal and Thin Film Preparation, Dr. Nikolai Kolesnikov (Ed.), ISBN: 978-953-307-610-2, InTech, Available from: http://www.intechopen.com/books/modern-aspects-of-bulk-crystal-and-thin-film-preparation/three-scale-structure-analysis-code-and-thin-film-generation-of-a-new-biocompatible-piezoelectric-ma

INTECH
open science | open minds

InTech Europe
University Campus STeP Ri
Slavka Krautzeka 83/A
51000 Rijeka, Croatia
Phone: +385 (51) 770 447
Fax: +385 (51) 686 166
www.intechopen.com

InTech China
Unit 405, Office Block, Hotel Equatorial Shanghai
No.65, Yan An Road (West), Shanghai, 200040, China
中国上海市延安西路65号上海国际贵都大饭店办公楼405单元
Phone: +86-21-62489820
Fax: +86-21-62489821

© 2012 The Author(s). Licensee IntechOpen. This is an open access article distributed under the terms of the Creative Commons Attribution 3.0 License, which permits unrestricted use, distribution, and reproduction in any medium, provided the original work is properly cited.

IntechOpen

IntechOpen